Title

Three-dimensional nanocable arrays with a copper core and cupric oxide shell for high power lithium ion batteries

Journal

RSC Advances, 3(29)

ISSN

2046-2069

Authors

Liu, Hao

Meng, Ying Shirley

Li, Quan

Publication Date

2013

DOI

10.1039/c3ra41460d

Peer reviewed

RSC Advances

RSC Publishing

PAPER

View Article Online
View Journal | View Issue

Cite this: *RSC Advances*, 2013, **3**, 11586

Three-dimensional nanocable arrays with a copper core and cupric oxide shell for high power lithium ion batteries

Hao Liu,[a] Ying Shirley Meng[b] and Quan Li*[a]

Received 26th March 2013,
Accepted 18th April 2013

DOI: 10.1039/c3ra41460d

www.rsc.org/advances

CuO is an attractive anode material for Li-ion batteries because of its high specific capacity. However, conventional CuO powders suffer from a large volume expansion during the Li insertion–extraction process, resulting in contact loss between the active material and the current collector. In this work, a nano-architecture made of metallic Cu core–CuO shell nanocable arrays is fabricated directly on a metallic collector by partial oxidation of three-dimensional Cu nanowire arrays. This type of binder/additive free electrode achieves a high specific capacity (840 mA h g^{-1} at 0.1 C) and excellent capacity retention ability (~600 mA h g^{-1} after 200 cycles at 0.5 C). The improved cyclic stability is attributed to its excellent adhesion of the active material on the current collector and short ionic/electronic transport pathways during cycling.

Introduction

Transition-metal oxides (such as CoO, CuO, NiO *etc.*) allow the incorporation of more than one Li atom per 3d transition metal, and thus exhibit large reversible specific capacities during the conversion reaction with Li. They are promising anode materials for Li-ion batteries.[1–5] Among those oxides, CuO is an attractive electrode for a Li-ion battery anode, due to its high specific capacity (a theoretical capacity of 670 mA h g^{-1}, being about twice as that of commercial graphitic carbon), and low cost.[2,3] However, the cyclability of the CuO anode is mainly limited by its large volume expansion (~174%) during the Li insertion and extraction process.[6] This volume expansion induces severe mechanical strain, causing damage to the integrity of the electrode architecture (by forming cracks *etc.*), and thus ineffective contact between the active material and the current collector.

Using a nanomaterial is an effective method to reduce battery capacity decay.[4,7,8] This is because nanostructured architectures are usually comprised of a large amount of void space, which can accommodate the volume expansion of the active materials during charge–discharge cycling. In addition, the diffusion lengths of the charge carriers (ions and electrons) can also be shortened in nanostructures. Inspired by such an idea, a number of CuO nanostructures, such as nanoparticles,[2] nanowires,[9] and hollow structures[5] have been investigated. However, the CuO nanostructures reported in these works are usually mixed with binders and additives before being tape-casted on a flat current collector. The introduction of binders and additives not only reduces the energy density of the electrode, but also generates undesired interfaces between the active materials and the additives, which increases the complexity of the charge transfer process.[10]

To tackle the above problems, a three-dimensional (3D) current collector–active material configuration has been recently proposed in several other material systems.[4,11,12] In an ideal configuration, the nano-active materials are deposited directly onto the 3D current collector to ensure good electrical and mechanical contact between them. The large surface to volume ratio of the nanostructured current collector ensures adequate hosting spots for the active materials, and the direct contact between the two provides efficient charge carrier transport routes.

In the present work, a 3D Cu core–CuO shell nano-architecture is designed. Metallic Cu nanowire arrays on a conductive substrate were first obtained, followed by their partial oxidization to CuO, which serves as an active material in the battery anode. The metallic Cu core–CuO shell nanocable array grown on the Ni anode was fabricated into coin-type cells. We observed considerable improvement in electrochemical performance when compared to its thin film and nanofiber (without Cu core) counterparts.

[a]*Department of Physics, The Chinese University of Hong Kong, Shatin, New Territory, Hong Kong E-mail: liquan@phy.cuhk.edu.hk; Fax: +852 39435204; Tel: +852 39436323*

[b]*Department of NanoEngineering, University of California San Diego, 9500 Gilman Drive, La Jolla, CA 92093, USA. E-mail: shirleymeng@ucsd.edu; Fax: +1 858 534 9553; Tel: +1858 822 4247*

Experimental

Preparation of the metallic Cu core–CuO shell structure on a conductive substrate

Firstly, metallic Cu nanowire arrays were obtained on a conductive substrate by cathodic electrodeposition with the aid of an anodic aluminum oxide (AAO) template.[4] Briefly, a polished Ni foil cathode, AAO (pore size 200 nm, Whatman), filter paper (mean porous diameter 20 μm, Whatman), and a Cu foil anode were first compressed tightly as a stack by an external force. The stack was then immersed into an electrolytic bath consisting of 100 g L^{-1} $CuSO_4 \cdot 5H_2O$, 20 g L^{-1} $(NH_4)_2SO_4$, and 80 mL L^{-1} diethylenetriamine (DETA). A two-step pulsed cathodic current profile (−0.002 A, 0.25 s, −0.03 A, 0.05 s, 20 000 cycles) was used to deposit the Cu nanowire arrays. After that, the AAO template was removed by 3 M NaOH.

Secondly, the Cu nanowire arrays were partially oxidized to CuO by an alkaline solution, consisting of 50 μL ammonia and 100 μL 1 M NaOH in 20 mL de-ionized water (pH ~11.3).[13] In this process, the Cu nanowire acted as the Cu source for the active material. Therefore, no additional Cu sources were required in the reaction. After the oxidation, a black surface finish was observed by the naked eye. The Ni substrate cannot be oxidized in this alkaline solution due to its notable resistance to attack by aqueous caustic alkalis.[14]

Preparation of CuO nanofibers or CuO thin films on a conductive substrate

In order to find out whether adjusting the morphology of the metallic nanowire array–active materials would benefit the electrochemical properties, two other configurations were also designed and fabricated. One was a CuO nanofiber which grew on a conductive substrate directly. Briefly, a thin layer of Cu was electrodeposited on a Ni substrate, followed by oxidization to form CuO using an alkaline solution. The other configuration was a CuO thin film grown on a conductive substrate. The thin film was fabricated on a Ni substrate by constant anodic current electrodeposition (1 mA cm^{-2}). The electrolytic bath consisted of 49.9 g L^{-1} $CuSO_4 \cdot 5H_2O$, 30 g L^{-1} tartaric acid, and 120 g L^{-1} NaOH.[15] These three different configurations are denoted as CuO-I (metallic Cu core–CuO shell on Ni substrate), CuO-II (CuO nanofiber on Ni substrate), and CuO-III (CuO thin film on Ni substrate), respectively.

Characterization

The composition and phases of the samples were examined by X-ray diffraction (XRD, SmartLab, Rigaku) with a Cu-Kα radiation source (d = 0.1541 nm). The morphologies and elemental analyses were characterized by a field emission scanning electron microscope (FESEM, Quanta 200, FEI), equipped with an energy-dispersive X-ray detector (EDX, Oxford). Transmission electron microscopy (TEM) measurements were also carried out with a Tecnai F20 (FEI) microscope operating at 200 kV.

Electrochemical properties of Li-ion batteries made with the Cu–CuO anode

The electrochemical properties of the samples were characterized by using CR2032 coin-type cells with Li foil as a counter electrode. The liquid electrolyte was 1.0 M $LiPF_6$ in the mixture of 1 : 1 (by volume) ethylene carbonate and diethyl carbonate (Novolyte Co.). No binder or conducting carbon was used. The coin cells were assembled in an argon-filled dry glove box (Labstar, M. Braun Inertgas Systems Co., Ltd.). Galvanostatic charge and discharge cycles were tested between 0.02 and 3.0 V at different rates on a multichannel battery test system (CT2001A, LAND batteries testing system, Wuhan Kingnuo Electronic Co., Ltd.). The electrochemical impedance spectroscopy (EIS) of the batteries was tested in the frequency range from 100 kHz to 0.05 Hz under an alternating current (AC) stimulus with a 5 mV amplitude (CHI 660C, Shanghai Chenhua Instrument Co., Ltd.). The impedance data were fitted using the ZView program.

Mass calculation of the active materials

To determine the mass of the active materials on the substrate, the samples were weighed before and after the formation of CuO by a semi-micro analytical balance (AEG-80SM, Shimadzu, readability: 0.01 mg). In the chemical oxidation process using Cu nanowire arrays or Cu foil to form the CuO (the samples of CuO-I or CuO-II), the metallic Cu nanowire is the sole Cu source and the O element comes from the alkaline solution. Therefore, the difference X in mass before and after the oxidation should only come from the O atoms in the CuO (the Ni substrate remained unchanged in this alkaline solution). The mass, Y, of CuO can then be calculated based on the mass fraction of O, using the equation,

$$Y = (16.0 + 63.5) \times X/16.0 = 4.97 \times X$$

For CuO-III, the difference in mass was contributed by the active materials. The weights of the active material of these three configurations were similar in the electrochemical test (Table 1). In the CuO-I sample, the percentage is ~51% by weight of the amount of the active material in the electrode [CuO/(CuO + residual Cu nanowire)].

Results and discussion

Fig. 1 shows the SEM image of the Cu nanowire arrays. The average diameter of Cu nanowires is ~200 nm, and the separation distance between the individual wires is ~130 nm. These parameters are inherited from the pore diameter and separation distance of the AAO template. The length of the Cu

Table 1 Mass calculation of the active material

Sample	Mass of O atoms (μg)	Mass of CuO (μg)
CuO-I	96	477
CuO-II	87	432
CuO-III	—	531

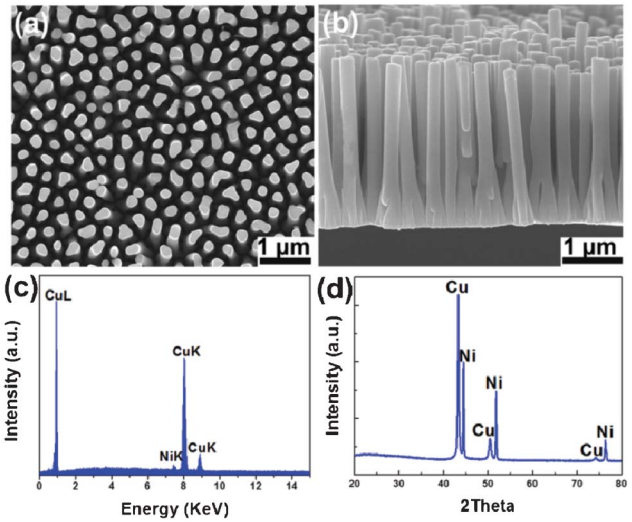

Fig. 1 SEM images of Cu nanowires from (a) top-view; and (b) side-view. (c) EDX taken from the nanowire array sample. (d) XRD θ–2θ scan of the same sample.

nanowires can be easily controlled in the range of several hundreds of nanometers to tens of microns by the duration of electrodeposition. Here, we show the nanowire arrays with a length of ~2.7 μm (Fig. 1b).

Only Cu and Ni signals are detected in the EDX spectrum (Fig. 1c), whereby the Ni signal comes from the Ni substrate. The crystallinity of the Cu in the nanowire arrays is determined by XRD. Other than those from the Ni diffractions, the rest of the diffraction peaks can be indexed to the cubic Cu (JCPDS No. 4-836). The relatively wide diffraction peaks suggest the small grain size of the Cu in the nanowire, which is estimated as 20 nm using the Scherrer equation. Chemical oxidation of the Cu nanowires leads to the formation of monoclinic CuO, while the original cubic Cu is not fully consumed, as disclosed by the X-ray diffraction (Fig. 2b). Fig. 2a shows the morphology of the Cu nanowires after oxidation. The straight array morphology is no longer clear due to the significant roughening of the surface of the original Cu nanowires. Nonetheless, the Cu nanowire is actually preserved, as revealed by the TEM images taken from such a sample (Fig. 2c and 2d). Despite the surface roughness due to oxidation, the dark contrast in the middle of the nanowires indicates the remaining Cu core (two nanowires arranged in parallel were shown in the image). To confirm the existence of the Cu core, EDX mapping of the nanowire was taken, as shown in Fig. 2e–g. It clearly shows the abundance of the Cu element at the core and the co-existence of Cu and O around the shell.

Further evidence of the existence of the Cu core comes from the etching experiments, when CuO is etched off by 10% HCl. When the surface CuO was completely removed, the nanowire core was revealed. Fig. 3a shows the SEM image of the residual Cu nanowires with a rough surface after the etching process. Their diameter is reduced to ~50–150 nm. The EDX (inset of

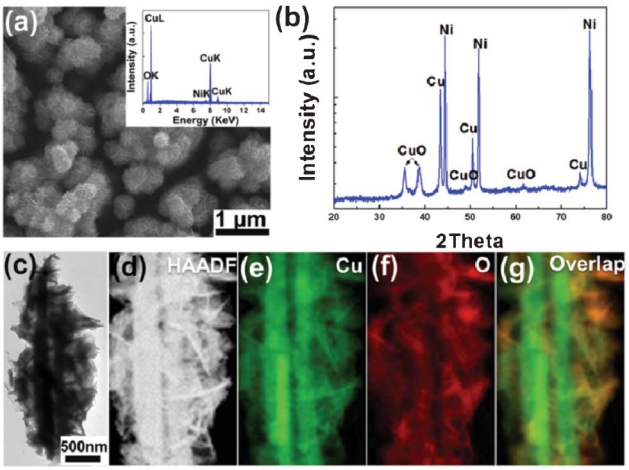

Fig. 2 (a) SEM image of the Cu core–CuO shell nanostructure (sample CuO-I). The inset shows the EDX spectrum taken from the same sample. (b) XRD θ–2θ scan of the same sample disclosing the presence of Cu and CuO in the sample (Ni signal comes from the substrate). (c) TEM image of the typical Cu core–CuO shell nanostructure. (d) High angle annular dark field (HAADF) image taken from part of the core–shell nanostructure. (e)–(g) EDX elemental mapping taken from the sample show in (e) map of Cu; (f) map of O; and (g) the overlap images of Cu and O showing their spatial distribution characteristics.

Fig. 3a) and XRD (Fig. 3b) spectra also confirm the absence of any oxide phase after etching.

To examine the effect of nanostructure morphology on the electrochemical properties, we have synthesized nanostructures of two other configurations—nanofibers without a metallic core (CuO-II) and a thin film (CuO-III). Fig. 4 shows the morphologies of the CuO-II and CuO-III samples. Sample CuO-II is obtained after chemical oxidation of the electrodeposited Cu film (Fig. 4a). The Cu thin film is covered with a large amount of CuO clusters mixed with long nanoribbons, as revealed by Fig. 4b. The length of a typical nanofiber is about 20 μm. In contrast, the surface of the CuO thin film (thickness ~840 nm) electrodeposited directly on the Ni substrate is rather flat (Fig. 4c). The XRD spectra confirm the formation of the CuO phase in both CuO-II and CuO-III (Fig. 4d).

Fig. 5a shows the galvanostatic charge–discharge profiles of the CuO-I/Li half-cell between 0.02 and 3.0 V at 0.05 C rate and

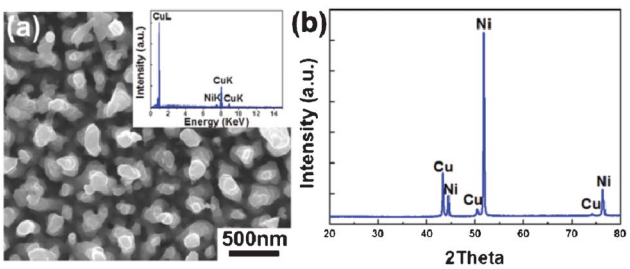

Fig. 3 (a) SEM image of the residual metallic Cu core after etching off the CuO-I sample. The inset shows the EDX spectrum of the residual metallic Cu nanowire. (b) XRD θ–2θ scan of the same sample showing the complete removal of the CuO phase.

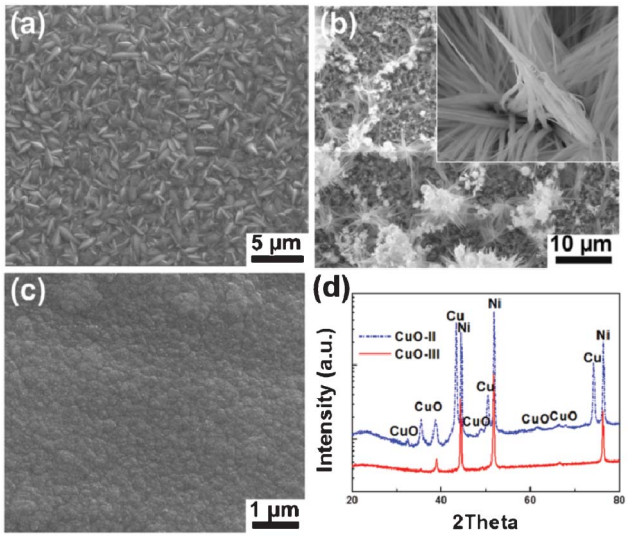

Fig. 4 SEM images of (a) an electrodeposited Cu film on the Ni substrate; (b) CuO cluster–nanofibers (CuO-II) obtained after chemical oxidation of the Cu film. A magnified image of a typical nanofiber is shown in the inset; (c) electrodeposited CuO thin film (CuO-III). (d) XRD θ–2θ scan of the CuO-II and CuO-III samples.

0.1 C rate. The initial discharge and charge capacities at the 0.05 C rate are 1550 and 864 mA h g^{-1}, respectively. After several cycles, the reversible capacities are stabilized around 840 mA h g^{-1}, even when the charging rate changes to 0.1 C. The complete reduction of CuO to metallic Cu requires 2 Li ions, corresponding to its theoretical capacity of 670 mA h g^{-1}. Therefore, the amount of Li ions reacted with one unit of CuO at different discharge states can be calculated. Since 4.7 Li ions (capacity 1550 mA h g^{-1}) react in the first discharge process, only 2.6 Li ions are removed in the subsequent charging process.

To better understand the conversion process during cycling, potentionstatic differential capacity–voltage curves are derived from Fig. 5a, as shown in Fig. 5b. In the first circle, four cathodic peaks are observed at 1.96, 1.30, 0.97, and 0.73 V *vs.* Li^+/Li, respectively. The first three peaks correspond to the phase change from CuO firstly to a solid solution of $Cu^{II}_{1-x}Cu^{I}_{x}O_{1-x/2}$ ($0 \leqslant x \leqslant 0.4$), then to Cu_2O, and lastly the formation of Cu and Li_2O, respectively. The fourth peak corresponds to the growth of an organic layer or solid electrolyte interphase (SEI) layer due to electrolyte decomposition.[2,9] In the first charging process, a broad peak located near

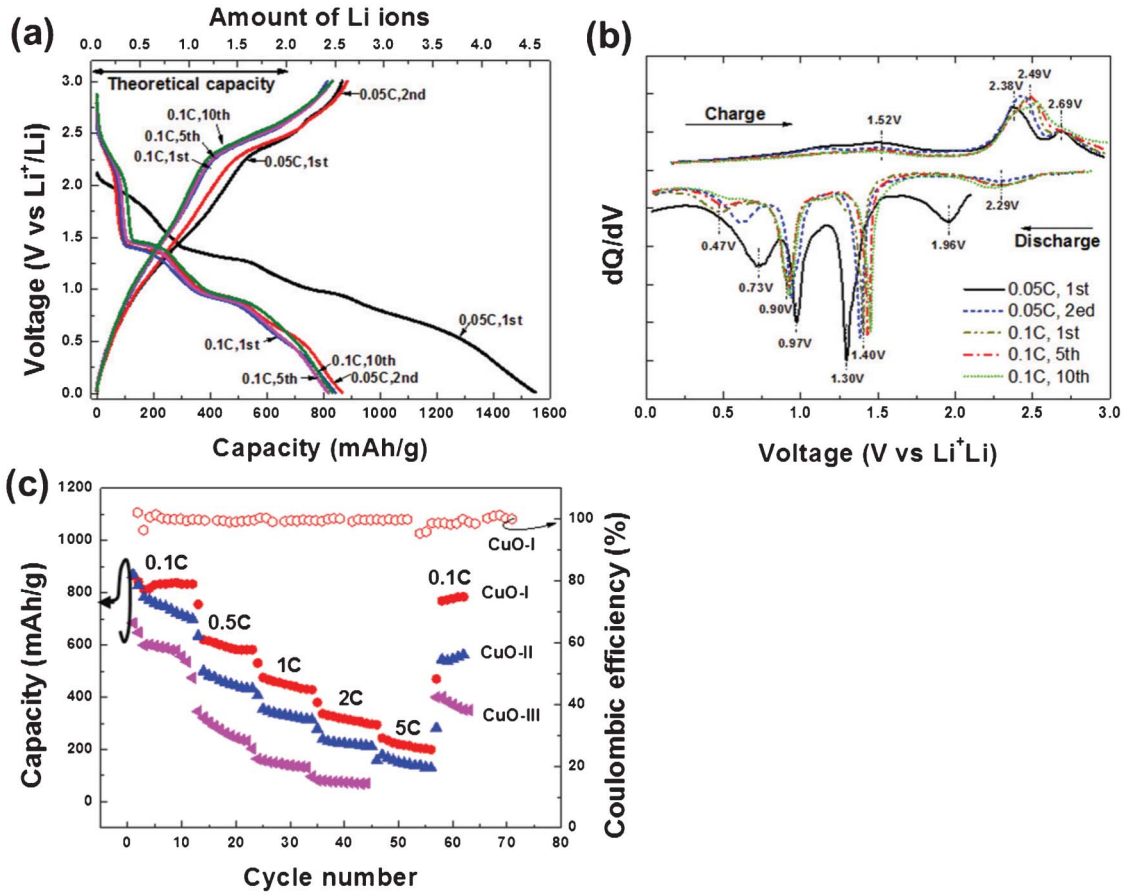

Fig. 5 (a) Voltage profiles of the first and second galvanostatic cycles at the 0.05 C rate, and the first, second and fifth galvanostatic cycles at the 0.1 C rate. The amount of Li ions reacted with one unit of CuO at different discharge states is calculated, as indicated by the top axis. (b) Potentiostatic differential capacity–voltage curves derived from Fig. 5a. (c) Charge rate capabilities of the CuO-I, CuO-II, and CuO-III electrodes.

1.52 V *vs.* Li^+/Li is indexed to the oxidation of the SEI layer. The other two peaks correspond to the formation of Cu_2O (2.38 V *vs.* Li^+/Li), and the partial oxidation of Cu_2O to CuO (2.69 V *vs.* Li^+/Li), respectively. In the second cycle, the cathodic peaks shift to 2.29, 1.38, 0.94, and 0.62 V *vs.* Li^+/Li, while the anodic peaks only change slightly. In the following cycles (0.1 C rate), there is no substantial change in the peak potentials except the peaks corresponding to the formation of the SEI layer. In the discharge process, such SEI layer related peaks shift to 0.47 V *vs.* Li^+/Li with a slow decrease in the peak intensity, indicating less and less of the newly formed SEI layer in continuous cycles. This suggests the stabilization of the SEI layer after several discharge and charge cycles.

In the first discharge process, more than 2 Li ions react (Fig. 5a). Débart *et al.* have pointed out that the growth of an organic-type surface layer on nanoparticles is one reason that is responsible for the extra capacity in the first discharge process.[2] In addition, excess Li ions may be accommodated in the boundary regions between nanosized metal and Li_2O grains; such a phenomenon has been observed in other transition metal oxide electrodes.[16,17]

In the subsequent charging process, only 2.6 Li ions are removed. The large irreversible capacity in the first cycle is mainly due to the irreversible process of formation of the SEI layer.[2] The use of nanomaterials also drastically increases the area of the surface which should be passivated by the SEI layer in the first cycle, resulting in the increasing amount of Li loss. However, the formation of the SEI layer greatly depends on the type of electrolyte. This problem would be mitigated if an appropriate electrolyte (*e.g.* ionic liquid type of electrolyte) is chosen. In this paper, we mainly focus on the design of the electrodes and the study of their electrochemical properties. The selection and discussion of the electrolyte is beyond the scope of this paper. In addition, the coexistence of Cu, Cu_2O, CuO, and an amorphous Li_2O phase observed in full charge state, suggests partial oxidation of Cu to Cu_2O and CuO, which may also contribute to some loss of capacity.[2]

Fig. 5c compares the rate capability of three different CuO anodes. The CuO-I electrode exhibits higher capacities than those of the other two at all charging rates. At the low rate of 0.1 C, the CuO-I electrode achieves a stable capacity of 840 mA h g^{-1}, while the CuO-II and CuO-III electrodes show about 780 and 680 mA h g^{-1}, with a rapid decay. Although the capacities decrease gradually when the charge rate increases from 0.5 C to 5 C, the CuO-I electrode always delivers the highest capacity among the three. In addition, the decayed capacity of the CuO-I electrode, after a high charge–discharge rate (5 C), is recoverable to about 790 mA h g^{-1}, when the rate returns to 0.1 C, suggesting good capacity retention.

The superior performance of the CuO-I anode, among the three, benefits greatly from its 3D configuration. On one hand, the 3D nano-architecture supplies a high surface area with a short length for both ion diffusion and electron transfer. These features make the transfer of carriers more efficient, leading to higher capacities than that of the thin film anode (CuO-III). On the other hand, the porous 3D network provides

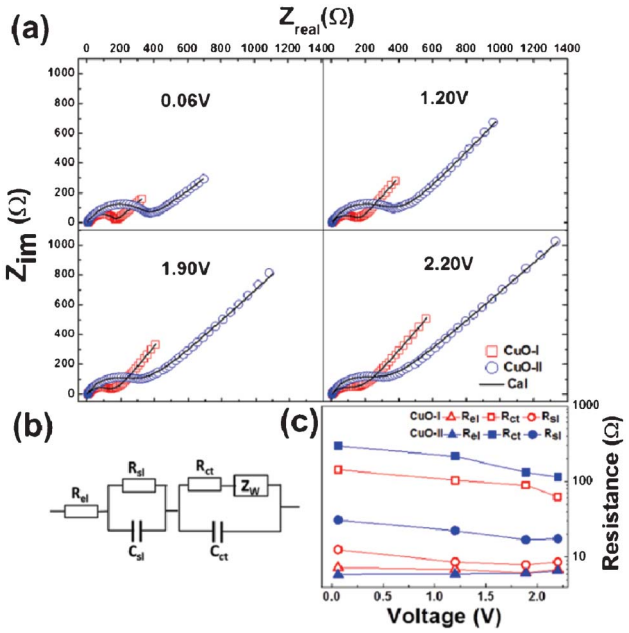

Fig. 6 (a) Nyquist plots of the CuO-I and CuO-II electrodes at different charge states during the first cycle. Square and circle symbols indicate experimental data of the CuO-I and CuO-II electrodes, respectively. (b) Equivalent circuit model for the CuO electrodes. R_{el} stands for solution resistance. R_{sl} and C_{sl} represent surface layer resistance and capacitance, respectively. R_{ct} and C_{ct} indicate charge transfer resistance and double layer capacitance, respectively. Z_w represents the Warburg impedance. The lines in Fig. 6a are the curves simulated using this model. (c) Calculation of the electrical parameters (R_{el}, R_{ct}, and R_{sl}) using the same model.

better accommodation to the volume change, which is induced by the Li insertion or extraction during the discharge or charge cycles. This characteristic enhances the mechanical stability of the cell and thus the stable contact between the active battery material and the electrode. As a result, such an electrode does not suffer from capacity decay as much as that of the thin film electrode (CuO-III).

Although both employ a 3D nano-architecture, the capacity of the CuO-I electrode is also higher than that of the CuO-II electrode at various discharge and charge rates. In the cable-like configuration of the CuO-I electrode, the metallic Cu core itself is a 3D current collector, making the transfer length of charge carriers even shorter than that in CuO nanowires. At the same time, the Cu nanowire core also serves as a good mechanical support for the active material, providing a stable contact between the active material and the current collector.

To further understand the origin of the different capacities of these two kinds of electrodes, EIS measurements were carried out at the potential range 0.06–2.20 V during the charging process, and the Nyquist plots are shown in Fig. 6a. All of them consist of a depressed semicircle and an inclined line. Generally speaking, a typical Nyquist plot of LIBs consists of three characteristic features: two depressed semicircles in the high and medium frequency range, followed by an inclined line in the low frequency region. The first depressed semicircle at high frequency responds to the resistance of the surface-

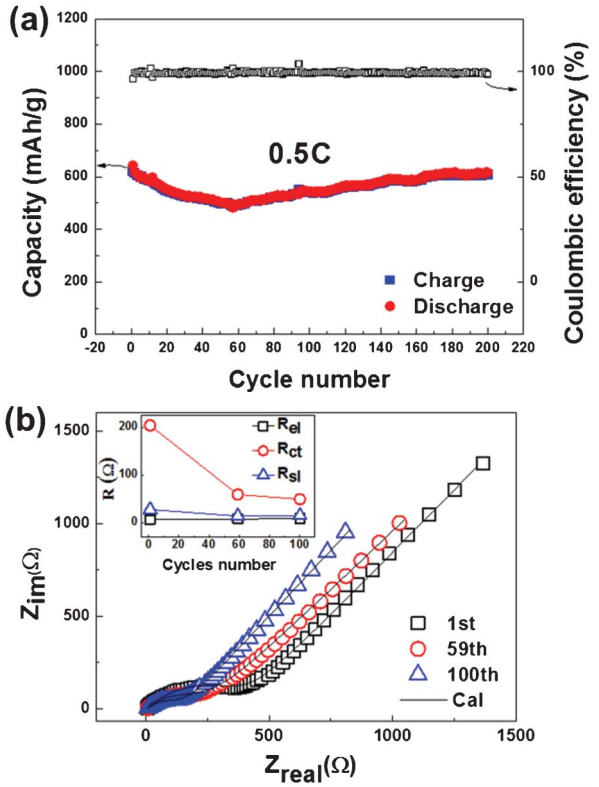

Fig. 7 (a) Cycling characteristic of the CuO-I electrode at 0.5 C rate. (b) Nyquist plots of the same electrode obtained at ~3.0 V in different charge cycles. The inset shows the calculated data of R_{el}, R_{sl}, and R_{ct}, respectively.

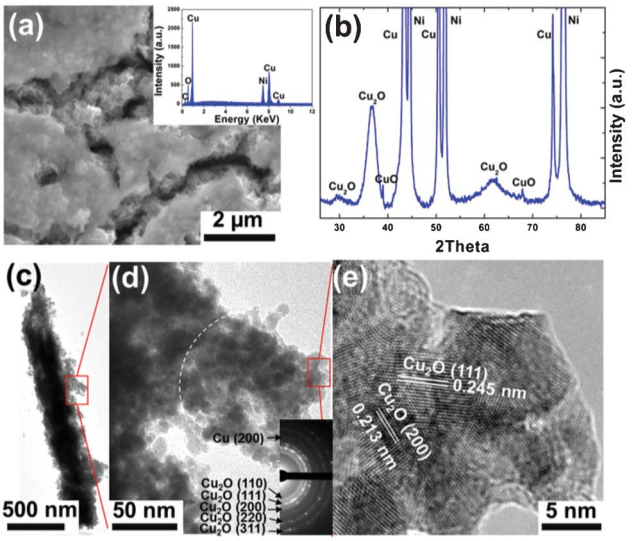

Fig. 8 (a) SEM image of the CuO-I electrode at the delithiation state. The inset shows the EDX spectrum of this sample. (b) XRD θ–2θ scan of the same sample. TEM images of a typical nanowire taken from the same sample (c) low magnification; (d) high magnification. The inset is the SAED pattern taken from the white circular region. (e) HRTEM image taken from Fig. 6d.

passivating layer (SEI layer). The second depressed semicircle at medium frequency is related to the resistance of the charge transfer on the electrode–electrolyte interfaces. The inclined line at low frequency represents the diffusion of the Li ion in the electrode, which is also named the Warburg impedance.[18] The single depressed semicircle in Fig. 6a thus indicates the high-frequency semicircle and medium-frequency semicircle overlap with each other. An appropriate equivalent circuit model (Fig. 6b) is established to simulate the Nyquist curves. The electrical parameters (*e.g.* R_{el}, R_{sl}, and R_{ct}) in this model can be calculated, as shown in Fig. 6c. The simulated results suggest a stable resistance of the electrolyte, while resistances from both charge transfer and surface layer of the CuO-I and CuO-II electrodes decrease in the charging process. Moreover, both the charge transfer resistance and surface layer resistance of the CuO-II electrode are about twice those of the CuO-I electrode. This could be another reason responsible for the better performance of the CuO-I electrode.

The cycling performance of the CuO-I anode was tested at the discharge–charge rate of 0.5 C, as shown in Fig. 7a. The initial capacity is about 640 mA h g^{-1}. It then drops gradually to 490 mA h g^{-1} during the first 60 cycles. In the subsequent cycles the capacity increases and stabilizes at about 610 mA h g^{-1} after the 170th cycle. The coulombic efficiency is ~99.5% in the cycling test. Those values of the cycling performance and the coulombic efficiency are higher than most reported CuO anodes consisting of nanorods,[19] networks,[20,21] nanoribbons,[22] and hollow structures.[5,23] The unique nanocable structure provides both the electron conductive pathway, as well as superior mechanical stability. In addition, the Nyquist plots of the CuO-I electrode are obtained at ~3.0 V from the 1st, 59th, and 100th charge cycles. Those data were also fit using the equivalent circuit model (Fig. 6b). Based on the data fitting simulation, the charge transfer resistances are found to decrease significantly, while little change in the resistances of both the surface layer and electrolyte are observed during the cycling test (Fig. 7b).

In order to identify the structural origin of such a cycling performance, the morphology, composition, and phases of the electrode are examined at full-delithiation (Fig. 8) and full-lithiation (Fig. 9) states after hundreds of cycles. The coin cell was held at 3 V or 0.01 V for 20 h before disassembly, in order to remove or insert Li ions as much as possible. Fig. 8a is a SEM image after delithiation. A thick layer is observed on the surface, which is the SEI layer. XRD analysis indicates the main crystalline phase is Cu_2O at a full-delithiation state after several hundred cycles (Fig. 8b). This is also consistent with the potentiostatic differential capacity *versus* voltage analysis (Fig. 5b). The decreasing tendency of the peak intensity at 2.69 V indicates that the partial oxidation of Cu_2O to CuO becomes more and more difficult during the charging process. Moreover, the average grain size of Cu_2O is estimated at about 5 nm using the Scherrer equation, which is much smaller than that of CuO (~20 nm) before the charge–discharge reaction. Further information on the microstructure is obtained from TEM (Fig. 8c, 8d and 8e). The grain size is found to be around 5 nm, which is consistent with the XRD result. The selection area diffraction pattern (SAED) taken from the shell shows

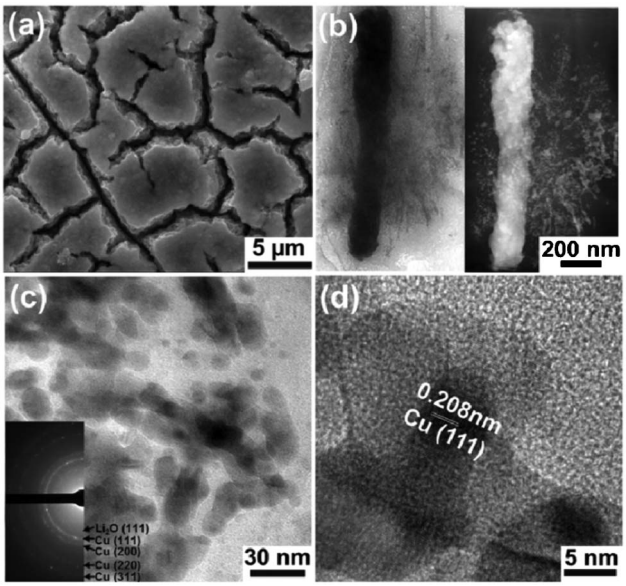

Fig. 9 (a) SEM image of the CuO-I electrode at the lithiation state. (b) Low magnified TEM image (left) and HAADF image (right) of a typical metallic core–cotton-like shell structure. (c) High magnified TEM image taken from the shell region in Fig. 9b. The inset shows the SAED pattern of the whole area of Fig. 9c. (d) HRTEM image taken from Fig. 9c.

diffraction rings that can be indexed to Cu_2O and Cu (Fig. 8d). A high-resolution TEM (HRTEM) image (Fig. 8e) reveals the lattice structure of the Cu_2O grains. The measured *d*-spacing of the lattices are ~0.25 nm and ~0.21 nm, corresponding to the (111) and (200) plane of cubic Cu_2O, respectively.

Fig. 9a is the SEM image after lithiation. A thick SEI layer can also be observed on the surface of the overall nano-architecture. In addition, as shown in the TEM image (Fig. 9b), a cotton-like structure is formed, adhering onto the dark Cu core. Therefore, the metallic core–active material shell structure is preserved during cycling, maintaining the mechanical stability of the electrode. The HAADF image indicates that some particles (high contrast spot) with a size of 5–10 nm (Fig. 9c) are embedded in the cotton-like structure. SAED confirms the cotton-like structure is the mixture of metallic Cu (high contrast spot in Fig. 9b) and Li_2O. In the HRTEM image (Fig. 9d), the lattice-plane can be indexed as the (111) plane of cubic Cu. Those results are consistent with the literature.[2]

The microstructure analysis suggests two distinct changes during cycling. First of all, only a fraction of Cu_2O converts to CuO even at the full-delithiation state. This partially recoverable conversion leads the capacity decay of the CuO electrode at first, due to a smaller theoretical capacity of Cu_2O (372 mA h g^{-1}) than that of CuO (670 mA h g^{-1}). Secondly, the grain size of the active material decreases from ~20 nm to ~5 nm during the charge–discharge reaction, an effect known as the electrochemical milling effect. A similar phenomenon has also been observed in the Cu_2O–Li_2O composite electrode[24] and α-Fe_2O_3 electrode.[25] The smaller grain size induces more contact surface areas between the electrode and electrolyte, which will facilitate transfer of Li ions and electrons. Therefore, the impedance of the cell decreases during the charge–discharge reaction (Fig. 7b). On the other hand, the decreased grain size of the active material leads to more boundaries between the nanosized Cu and the Li_2O grains during the discharge process. These boundaries can help to store additional Li, resulting in the capacity rising after several tens of cycles until the electrochemical milling eventually stabilizes. As a result, the capacities of the CuO-I anode decrease at first and then increase with continued cycling (Fig. 7a).

Conclusions

A 3D Cu core–CuO shell nanocable array anode was fabricated by the controlled oxidation of Cu nanowire arrays in an alkaline solution. The metallic Cu nanowire arrays firstly provide the Cu source for the active material in the battery anode. During the charging–discharging process of the battery employing such a 3D anode, the Cu nanowire arrays provide not only mechanical support, but also electrically conductive pathways for the active materials. In addition, the porous nature of the 3D configuration also helps to accommodate the volume expansion of the active material during cycling. Consequently, the cable-like structure exhibits a considerable improvement of the electrochemical performance, as compared to its thin film or nanofiber counterparts. It achieves a high specific capacity (840 mA h g^{-1} at 0.1 C) and excellent capacity retention ability (~600 mA h g^{-1} after 200 cycles at 0.5 C). This method can be easily applied to other metal–metal oxide systems in general.

Acknowledgements

This work is supported by General Research funding of the Research Grants Council under project No. 414612. Y. S. Meng acknowledges the support of the American Chemical Society Petroleum Research Fund (51311-DNI10).

References

1 P. Poizot, S. Laruelle, S. Grugeon, L. Dupont and J. M. Tarascon, *Nature*, 2000, **407**, 496–499.
2 A. Débart, L. Dupont, P. Poizot, J. B. Leriche and J. M. Tarascon, *J. Electrochem. Soc.*, 2001, **148**, A1266.
3 W. Zhang, M. Li, Q. Wang, G. Chen, M. Kong, Z. Yang and S. Mann, *Adv. Funct. Mater.*, 2011, **21**, 3516–3523.
4 P. L. Taberna, S. Mitra, P. Poizot, P. Simon and J. M. Tarascon, *Nat. Mater.*, 2006, **5**, 567–573.
5 J. H. Ju and K. S. Ryu, *J. Electrochem. Soc.*, 2011, **158**, A814.
6 S. Gao, S. Yang, J. Shu, S. Zhang, Z. Li and K. Jiang, *J. Phys. Chem. C*, 2008, **112**, 19324–19328.
7 C. K. Chan, H. Peng, G. Liu, K. McIlwrath, X. F. Zhang, R. A. Huggins and Y. Cui, *Nat. Nanotechnol.*, 2008, **3**, 31–35.

8 L. F. Cui, Y. Yang, C. M. Hsu and Y. Cui, *Nano Lett.*, 2009, **9**, 3370–3374.
9 X. P. Gao, J. L. Bao, G. L. Pan, H. Y. Zhu, P. X. Huang, F. Wu and D. Y. Song, *J. Phys. Chem. B*, 2004, **108**, 5547–5551.
10 G. J. Nelson, B. N. Cassenti, A. A. Peracchio and W. K. S. Chiu, *J. Electrochem. Soc.*, 2012, **159**, A598–A603.
11 F. F. Cao, J. W. Deng, S. Xin, H. X. Ji, O. G. Schmidt, L. J. Wan and Y. G. Guo, *Adv. Mater.*, 2011, **23**, 4415–4420.
12 J. Hassoun, S. Panero, P. Simon, P. L. Taberna and B. Scrosati, *Adv. Mater.*, 2007, **19**, 1632–1635.
13 S. Anandan, X. Wen and S. Yang, *Mater. Chem. Phys.*, 2005, **93**, 35–40.
14 N. N. Greenwood and A. Earnshaw, *Chemistry of the elements*, Elsevier, 1997.
15 H. M. Kothari, E. A. Kulp, S. Boonsalee, M. P. Nikiforov, E. W. Bohannan, P. Poizot, S. Nakanishi and J. A. Switzer, *Chem. Mater.*, 2004, **16**, 4232–4244.
16 P. Balaya, H. Li, L. Kienle and J. Maier, *Adv. Funct. Mater.*, 2003, **13**, 621–625.
17 J. Maier, *Nat. Mater.*, 2005, **4**, 805–815.
18 J. Y. Xiang, J. P. Tu, Y. Q. Qiao, X. L. Wang, J. Zhong, D. Zhang and C. D. Gu, *J. Phys. Chem. C*, 2011, **115**, 2505–2513.
19 Z. Wang, F. Su, S. Madhavi and X. W. Lou, *Nanoscale*, 2011, **3**, 1618–1623.
20 H. Wang, Q. Pan, J. Zhao, G. Yin and P. Zuo, *J. Power Sources*, 2007, **167**, 206–211.
21 J. Y. Xiang, J. P. Tu, L. Zhang, Y. Zhou, X. L. Wang and S. J. Shi, *J. Power Sources*, 2010, **195**, 313–319.
22 F. S. Ke, L. Huang, G. Z. Wei, L. J. Xue, J. T. Li, B. Zhang, S. R. Chen, X. Y. Fan and S. G. Sun, *Electrochim. Acta*, 2009, **54**, 5825–5829.
23 Y. Hu, X. Huang, K. Wang, J. Liu, J. Jiang, R. Ding, X. Ji and X. Li, *J. Solid State Chem.*, 2010, **183**, 662–667.
24 Y. Yu, Y. Shi and C. H. Chen, *Nanotechnology*, 2007, **18**, 055706.
25 M. F. Hassan, Z. Guo, Z. Chen and H. Liu, *Mater. Res. Bull.*, 2011, **46**, 858–864.